

# Large Coupled Bending and Torsional Deformation of an Elastic Rod Subjected to Fluid Flow

Masoud Hassani<sup>a</sup>, Njuki W. Mureithi<sup>a</sup>, Frédérick P. Gosselin<sup>a,\*</sup>

<sup>a</sup>*Department of Mechanical Engineering, École Polytechnique de Montréal  
C.P. 6079, Succ. Centre-ville, Montréal, Québec, Canada H3C 3A7*

---

## Abstract

*In the present work, we seek to understand the fundamental mechanisms of three-dimensional reconfiguration of plants by studying the large deformation of a flexible rod in fluid flow. Flexible rods made of polyurethane foam and reinforced with nylon fibers are tested in a wind tunnel. The rods have bending-torsion coupling which induces a torsional deformation during asymmetric bending. A mathematical model is also developed by coupling the Kirchhoff rod theory with a semi-empirical drag formulation. Different alignments of the material frame with respect to the flow direction and a range of structural properties are considered to study their effect on the deformation of the flexible rod and its drag scaling. Results show that twisting causes the flexible rods to reorient and bend with the minimum bending rigidity. It is also found that the Vogel exponent of a reconfiguring rod is not affected by torsion. Finally, using a proper set of dimensionless numbers, the state of a bending and twisting rod is characterized as a beam undergoing a pure bending deformation.*

*Keywords:* Reconfiguration, Drag reduction, Torsion, Large deformation, Anisotropic rod

---

## 1. Introduction

In contrast to engineering structures, plants are generally flexible and deform significantly under fluid loading. This deformation typically causes drag reduction and is called *reconfiguration* in biomechanics (Vogel, 1984, 1989). Unlike rigid bluff bodies, the drag force on plants is not proportional to the square of the flow velocity. The drag force on flexible plants varies with the flow velocity as

$$D \propto U^{2+\theta}, \quad (1)$$

---

\*Corresponding author

Email address: frederick.gosselin@polymtl.ca (Frédérick P. Gosselin)

where  $\vartheta$  is the Vogel exponent. This exponent quantifies the effect of flexibility on the drag scaling and is typically negative for plants (Vogel, 1984). Plants reconfigure using two main mechanisms: frontal area reduction and streamlining. The more negative  $\vartheta$  is, the more the drag is reduced due to reconfiguration.

Many experimental drag measurements have been performed on trees (Vollsinger et al., 2005), crops (Sterling et al., 2003) and algae (Koehl & Alberte, 1988) whether in wind tunnels, water flumes or their natural setting. This was done to quantify the effect of streamlining and frontal area reduction on drag scaling. Understanding reconfiguration is necessary to predict or prevent the adverse effect of strong winds or water flows on plants such as windthrow, uprooting and lodging (Rudnicki et al., 2004; Berry et al., 2004). *Thigmomorphogenesis*, or the influence of mechanical stimuli such as wind loading on the growth of plants, is another area where a better understanding of plant-flow interaction can make a contribution (Niklas, 1998).

In general, plants are slender and a fundamental understanding of their reconfiguration has therefore been sought by modeling them as bending beams and plates (Alben et al., 2002, 2004; Gosselin et al., 2010; Luhar & Nepf, 2011; Gosselin & de Langre, 2011; Schouveiler & Boudaoud, 2006). A flexible beam undergoing bending due to flow is a simple academic representation of reconfiguration. For instance, the deformation and the drag of flexible glass fibers have been measured in a two-dimensional soap film flow which allows modeling and flow visualisation (Alben et al., 2002, 2004). To theoretically model the bending fiber in the soap film flow, the authors coupled the Euler-Bernoulli beam theory with an exact potential flow solution using the Helmholtz free streamline theory. Bending plates made of transparency films were also studied in a wind tunnel (Gosselin et al., 2010). Theoretical representation of these experiments was done by coupling a semi-empirical drag formulation and the Euler-Bernoulli beam theory.

Although bending beams and fibers capture the essence of the two-dimensional deformation of plants, they cannot represent all forms of reconfiguration. Other effects are important in reconfiguration and can influence the Vogel exponent such as: buoyancy (Luhar & Nepf, 2011), poroelasticity (Gosselin & de Langre, 2011), three-dimensional bending deformation (Schouveiler & Boudaoud, 2006). Moreover, the approach of using simple structures was also employed to study inelastic brittle reconfiguration, i.e., pruning (Lopez et al., 2011; Eloy, 2011).

While the aforementioned fundamental studies focus on bending deformation, torsion has been ignored in reconfiguration. However, it is known that plants twist significantly under fluid loading. For

Table 1: The average of twist-to-bend ratio for some natural and engineering structures

Species	Geometry	$\eta$	Reference
Isovolumetric material	circular	1.5	-
Metallic rod	circular	1.3	-
Daffodil stem	semi-circular	13.3	Vogel (2007)
Banana petiole	U-shape	68	Ennos et al. (2000)
Sedge stem	semi-triangle	65	Ennos (1993)
Tree trunk	semi-circular	7.34	Vogel (2007)

instance, the stem of a daffodil holds the flower horizontally and twists at the slightest breeze aligning the flower downwind thus reducing its drag (Etnier & Vogel, 2000). The trunks of trees with crown asymmetry also undergo significant twist under wind loading. Because of their fibrous construction, plants and trees are known to twist more easily than they bend (Vogel, 1992; Skatter & Kuera, 1997). This is quantified by the *twist-to-bend ratio*,

$$\eta = \frac{EI}{GJ}, \quad (2)$$

where  $EI$  is the bending rigidity and  $GJ$  is the torsional rigidity. High values of  $\eta$  represent a structure which can twist more easily than it can bend. Table 1 shows a comparison between the twist-to-bend ratios of some natural and engineering structures. In comparison to engineering structures, branches, petioles and stems have a significantly larger value of  $\eta$  (Vogel, 1992; Pasini & Mirjalili, 2006). Figure 1a shows a schematic of the U-shape cross section of a banana petiole with a large twist-to-bend ratio of 68. As a result, a banana leaf twists while bending downwind (see Fig. 1b and c). For comparison, a homogeneous and isotropic material with circular section has a twist-to-bend ratio equal to  $1+\nu$  or 1.3 for metallic materials assuming the Poisson's ratio is about 0.3 (Vogel, 1992).

Since many plants twist when subjected to flow, the following question arises: What is the effect of torsional deformation on the reconfiguration of plants and flexible structures, and how does it change their drag scaling, i.e., their Vogel number? The bending beams and plates of the previous studies cannot represent the torsional deformation of plants. Therefore a new approach is necessary to idealize plants with simple structures. In this paper, we consider the reconfiguration of an elastic rod which can twist and bend. A mathematical model is developed considering the arbitrary large deformation of a rod subjected to fluid flow. Tests are also done in a wind tunnel on flexible rods made of polyurethane foam with strategically placed reinforcements to tailor their twist-to-bend ratio and their twisting-bending coupling.

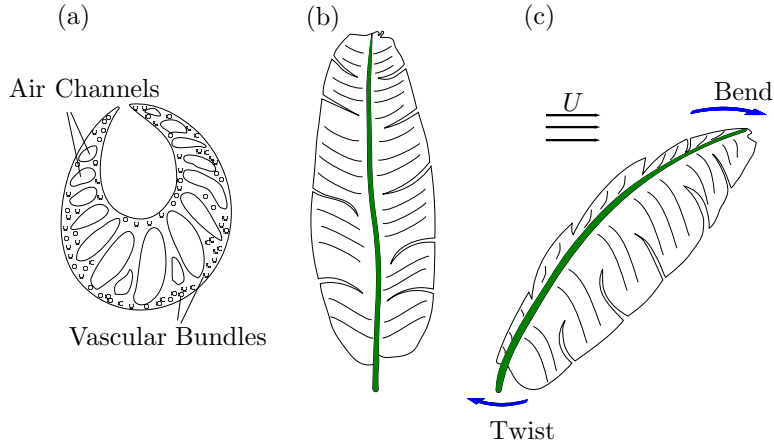


Figure 1: Schematics of a banana leaf (a) U-shape cross section of its petiole with a large twist-to-bend ratio; (b) upright banana leaf; and (c) leaf twisting to bend downwind. Inspired by Ennos et al. (2000).

## 2. Methodology

### 2.1. Experimental Procedure and Materials

The large deformation of a flexible rod bending and twisting under pressure drag is studied. The tests are performed in the closed-loop wind tunnel of the laboratory of Aerodynamics and Fluid-Structure Interactions at École Polytechnique de Montréal. The wind tunnel has a square test section of  $60 \times 60 \text{ cm}^2$  and can produce a maximum air speed of  $90 \text{ ms}^{-1}$ . Figure 2 shows the custom-made load measuring equipment used for the wind tunnel tests. The test setup consists of a force balance (3), a speed reduction gearbox (2), and a rotary servo motor (1) mounted on the gearbox. The 6-axis force balance (ATI GAMMA, ATI Industrial Automation, Apex, North Carolina) used in the present experiment, measures the aerodynamic forces in addition to the bending and twisting moments. The set of the servo, gearbox and force balance is mounted on an aluminum frame (4) and a wooden panel (5) which is used to support the setup on top of the wind tunnel. The rod (6) is fixed to the force balance inside the test section of the wind tunnel.

The ATI GAMMA force transducer was calibrated to measure a maximum 32 N of transverse loading, 100 N of axial loading and 2.5 Nm of torque and bending moments. The resolution of the force transducer is  $6.25 \times 10^{-3} \text{ N}$  for the transverse loading,  $12.5 \times 10^{-3} \text{ N}$  for the axial loading and  $0.5 \times 10^{-3} \text{ Nm}$  for the moments. From static tests with a calibration weight of 200 g, we estimate the precision of the static force measurement to be within 1 percent of the time-averaged reading. Moreover, in the wind tunnel tests, the standard deviation of the time fluctuating forces and moments, mainly due to turbulence buffeting, was evaluated to be between 4 and 10 percent of the time-averaged

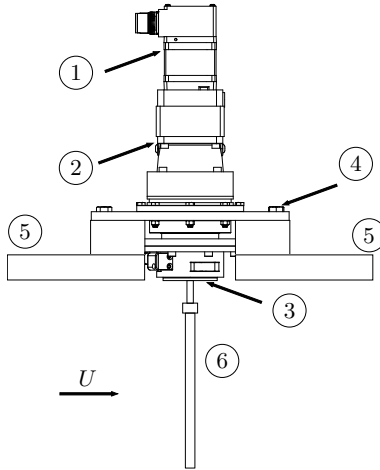


Figure 2: Schematic of the test setup installed on top of the wind tunnel. The setup consists of a servo (1), gearbox (2), force balance (3), aluminum frame (4), wooden panel (5) and a rod specimen (6).

measurement. For the velocity range of the present experiments, vortex shedding excitation is not significant because the predicted shedding frequency for a Strouhal number of 0.2 is more than 40 Hz while the fundamental frequency of the specimens is of the order of 1 Hz. Hence the measurements represent static values of the lightly fluctuating loads averaged over 30 seconds.

Rods are slender structures which can bend and twist. Rods with circular sections are used to simplify the geometry and the aerodynamic loading evaluation. For non-circular rods, fluid loading depends on the angle of each section of the rod with the flow direction i.e. the local angle of attack. The loading on a circular rod, however, is independent of the twist of the rod's sections. Moreover, the flow on a normal cylinder is on average symmetric and is not expected to generate a twisting moment. Coupling between torsional and bending deformation is achieved through *directional rigidity* which induces torsional deformation in a bending rod. This coupling gives rise to three-dimensional deformation. Herein, directional rigidity or asymmetric stiffness (De Goeij et al., 1999) refers to different bending rigidities in different directions.

Using this concept, composite rods are made using polyurethane foam and are reinforced in one direction using nylon fibers (see Fig. 3). Nylon fibers are pre-aligned along the axis of a non-stick Teflon tube. They are distributed along one diameter in the cross section of the rod to achieve directional rigidity. Two types of nylon fibers with different diameters and Young's moduli are used:  $d_f = 0.3$  mm and  $E_f = 3300$  MPa,  $d_f = 0.75$  mm and  $E_f = 2360$  MPa. The two-component polyurethane foam used (Flexfoam-iT, Smooth-on Inc., Easton, Pennsylvania) expands up to 6 times its original volume upon mixing. The mixture is poured and pressurized in the tube and left to harden over 4 to 5 hours.

The rigidity of the rod depends on the amount of foam inside the mold, diameter of the fabricated rod, thickness and the distance of the fibers from the rod’s neutral axis. Three-point-bending tests are performed to determine the bending rigidities in the  $x$  and  $y$ -directions (Fig. 3). The directions  $x$  and  $y$  construct a *material frame* defined with the alignment of the reinforcement fibers.

The torsional rigidity of the rod is determined by measuring the frequency of torsional oscillation of the rod attached to a heavy weight at one end and fixed at the other. The system is designed to oscillate around the rod’s centerline so the torsional rigidity is calculated from the measured frequency as  $GJ = LJ_m\omega_n^2$ . In this equation,  $J_m$  is the mass moment of inertia of the system around the rod’s centerline and  $\omega_n$  is the measured natural frequency of the rotational oscillation. Table 2 shows the characteristics of tested specimens made of polyurethane foam.

In the experimental study, the rod is attached to the 6-axis force balance on one end via a 10 cm mast and is free at the other end. Normally, a cantilever rod under transverse loading is considered to have a fixed position and slope at the fixed end. However, in our experiments, the rod is made of a soft material which cannot be easily clamped to maintain a constant slope at its fixed end when subjected to wind loading. Trying to clamp the fixed end of the foam rod pinches it, thus inducing a rotation about its fixed end instead of a smooth deformation along its length. To take into account this imperfection in the boundary condition, the fixed end is considered as a torsion spring in the mathematical model. The torsion coefficient of the spring ( $k_s$ ) is then evaluated using the measured in-plane bending moment and the rotation angle at the clamped end captured from photographs. A linear relation is considered between the in-plane bending moment and the rotation angle:

$$M_Y = k_s\alpha_s , \quad (3)$$

where  $M_Y$  is the in-plane bending moment at the clamped end while  $Y$  is perpendicular to the flow direction (Fig. 3). In addition,  $\alpha_s$  is the rotation angle at the clamped end.

The fixed end of the rod is rotated incrementally around its central axis in the wind tunnel using the servo motor shown in Fig. 2. This is done to expose different alignments of the reinforcement

Table 2: Physical properties of tested specimen

Specimen	$L$ (cm)	$d$ (cm)	$(EI)_y$ (Nm <sup>2</sup> )	$\frac{(EI)_y}{GJ}$	$\frac{(EI)_y}{(EI)_x}$	Weight (g)
R1	30	3.17	0.0563	1.00	0.41	120
R2	28	2.54	0.0262	1.26	0.24	65
R3	25	1.58	0.0033	1.20	0.21	20

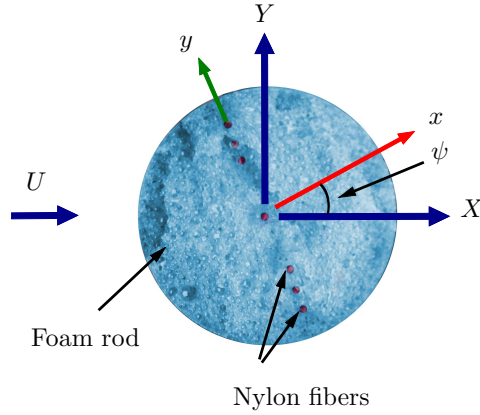


Figure 3: Photograph of a flexible rod's section made of polyurethane foam and reinforced with nylon fibers which have an angle of incidence  $\psi$  with the flow. The angle of incidence at the clamped end is defined by  $\psi_0$ .

direction at the clamped end with respect to the flow direction making an *angle of incidence*  $\psi_0$  (see Fig. 3). For each angle of incidence, the drag scaling is evaluated for a range of flow velocities. A variety of dimensions, structural rigidity and bending-torsion coupling are therefore considered to study the effects of various parameters on the deformation of the flexible rod and its drag scaling. Measurements are performed for flow velocities ranging from  $5 \text{ ms}^{-1}$  to  $65 \text{ ms}^{-1}$  and angles of incidence ranging from 0 to 90 degrees. The Reynolds number for the tests varies from approximately  $1.5 \times 10^4$  to  $10^5$  for R1 and R2 and from  $5 \times 10^3$  to  $6.5 \times 10^4$  for R3.

Images of the test specimens are captured in the wind tunnel using a DSLR camera. For the side view, a  $60 \times 60 \text{ cm}^2$  LED panel was placed behind the test specimen outside the wind tunnel to capture high contrast images with a white background. For the frontal view, the camera was installed inside the wind tunnel far upstream of the specimens. Consequently, due to the large wind loading on the camera inside the wind tunnel, it was not possible to capture front view images in high velocities.

## 2.2. Theoretical Model

An elastic rod is a three-dimensional slender structure (Audoly & Pomeau, 2010) where its length,  $L$ , is much larger than its two other dimensions. Kirchhoff's theory of rods is a classic theory considering finite displacements while assuming small strains (Dill, 1992). The rod is represented by a curve which can deform in three-dimensional space. It can also twist around this curve. The curve is defined as the centerline of the rod which is assumed *inextensible* (Audoly & Pomeau, 2010). It is assumed that each cross section of the rod remains planar and normal to the centerline. Bending moments are proportional to the curvatures,  $\kappa_x$  and  $\kappa_y$  and the twisting moment is proportional to the twist  $\tau$ .

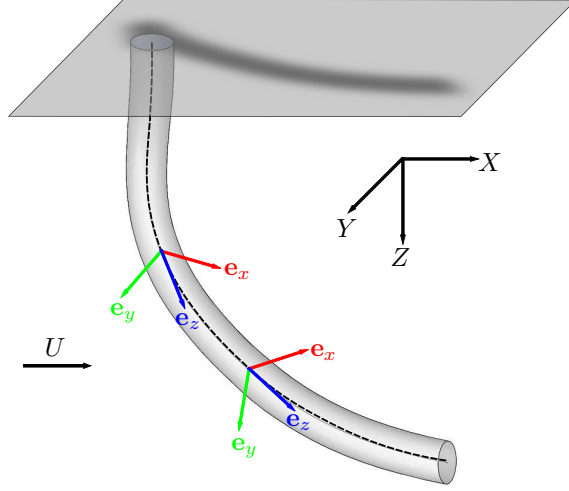


Figure 4: Schematic of a rod connected to a fixed coordinate system with moving material frame attached to its centerline.

The constitutive relation for a bending and twisting rod made of isotropic material is then written as (Audoly & Pomeau, 2010):

$$\mathbf{M} = (EI)_y \kappa_y \mathbf{e}_x + (EI)_x \kappa_x \mathbf{e}_y + GJ\tau \mathbf{e}_z . \quad (4)$$

where  $\mathbf{M}$  is the vector of internal moments.

To track the rod twist, a material frame is defined as a moving coordinate system connected to the centerline of the rod following its twist and deformation (Audoly & Pomeau, 2010). Herein, we represent this frame by three unit vectors  $\mathbf{e}_i(s)$  for  $i = x, y$  and  $z$ . Since the material frame moves and twists with the centerline of the rod,  $s$  is considered the distance in the curvilinear or Lagrangian coordinate system along the rod's centerline from its fixed end to its free end. The unit vector  $\mathbf{e}_z$  is tangent to the rod's centerline and  $\mathbf{e}_x$  and  $\mathbf{e}_y$  are principal directions of curvature in the cross sectional plane (Audoly & Pomeau, 2010) as illustrated in Fig. 4. Due to the assumption of small strains, the directions of the material frame are considered approximately orthonormal. The set comprising the centerline and the material frame is sometimes called the *Cosserat curve* (Audoly & Pomeau, 2010). The rod is connected to a fixed Eulerian coordinate system which is shown by  $X$ ,  $Y$  and  $Z$  with unit vectors  $\mathbf{e}_X$ ,  $\mathbf{e}_Y$  and  $\mathbf{e}_Z$  as illustrated in Fig. 4.

To evaluate the full state of a Kirchhoff rod, the rotation of the material frame around the centerline should be considered. The *direction cosines* are a representation of the material frame's rotation. They

form a transformation matrix  $[c(s)]$  relating the material frame to the fixed frame as:

$$\begin{Bmatrix} \mathbf{e}_x \\ \mathbf{e}_y \\ \mathbf{e}_z \end{Bmatrix} = \begin{bmatrix} c_{11} & c_{12} & c_{13} \\ c_{21} & c_{22} & c_{23} \\ c_{31} & c_{32} & c_{33} \end{bmatrix} \begin{Bmatrix} \mathbf{e}_X \\ \mathbf{e}_Y \\ \mathbf{e}_Z \end{Bmatrix}, \quad (5)$$

where  $c_{ij}$  is a direction cosine (Love, 1944). The three direction cosines of each row of the matrix  $[c]$  form a unit vector representing a direction of the material frame (Love, 1944). Consequently, six of the direction cosines are independent and the others can be calculated from these six independent ones. Alternatively to direction cosines, quaternions could have been used (Lazarus et al., 2013). Following the approach explained in detail by Audoly & Pomeau (2010), the spatial derivative of each direction of the material frame with respect to  $s$  is defined by:

$$\mathbf{e}'_x(s) = \tau(s)\mathbf{e}_y(s) - \kappa_y(s)\mathbf{e}_z(s), \quad (6a)$$

$$\mathbf{e}'_y(s) = -\tau(s)\mathbf{e}_x(s) + \kappa_x(s)\mathbf{e}_z(s), \quad (6b)$$

$$\mathbf{e}'_z(s) = \kappa_y(s)\mathbf{e}_x(s) - \kappa_x(s)\mathbf{e}_y(s), \quad (6c)$$

where a prime ( ' ) denotes a spatial derivative with respect to  $s$ . Using this approach, nine first order differential equations, six of which are independent, are derived (refer to Appendix 1).

The Kirchhoff equations for the equilibrium of forces and moments in a rod are written as:

$$\mathbf{F}'(s) + \mathbf{p}(s) = 0, \quad (7)$$

$$\mathbf{M}'(s) + \mathbf{e}_z(s) \times \mathbf{F}(s) + \mathbf{q}(s) = 0, \quad (8)$$

where  $\mathbf{p}(s)$  is the vector of external forces per unit length and  $\mathbf{q}(s)$  is the vector of external moments per unit length in the three directions of the material frame.  $\mathbf{F}(s)$  is the vector of internal forces, namely the shear forces  $N_x$ ,  $N_y$  and the axial tension  $T$ , i.e.,

$$\mathbf{F} = N_x\mathbf{e}_x + N_y\mathbf{e}_y + T\mathbf{e}_z. \quad (9)$$

Finally, by expanding Eqn. 7 and Eqn. 8 and using Eqn. 6, we obtain six separate differential equations which define the centerline curve of the rod.

The weight of the rod and the fluid loading are considered as external loading. The weight of

the rod is calculated as the rod's mass  $m$  times the gravitational acceleration  $g$  acting in the  $Z$ -direction. To evaluate the fluid loading on a deformed rod, we use Taylor's semi-empirical formulation (Taylor, 1952) of the pressure drag force on an oblique cylinder in three-dimensional flow. This method was used successfully in previous reconfiguration studies on bending beams (Gosselin et al., 2010; Luhar & Nepf, 2011). In the method, only the component of the flow velocity normal to the cylinder centerline contributes to the pressure drag force. The normal force on an oblique cylinder is proportional to  $\sin^2\theta$ , where  $\theta$  is the local angle that the cylinder centerline makes with the flow velocity vector. Without loss of generality, we consider a flow aligned with the  $X$ -axis, thus:

$$\cos\theta = \frac{\mathbf{e}_z \cdot \mathbf{e}_X}{|\mathbf{e}_z| |\mathbf{e}_X|} = c_{31} \ , \quad \sin\theta = \sqrt{1 - c_{31}^2} \ . \quad (10)$$

For Reynolds numbers ranging from  $10^3$  to  $10^5$ , the drag coefficient of a cylinder is nearly constant. Thus, the normal force per unit length on an oblique cylinder is calculated as:

$$p_n = \frac{1}{2} \rho d C_D (U \sin\theta)^2 \ , \quad (11)$$

where  $C_D$  is the drag coefficient obtained from experiments on rigid circular rods with the same aspect ratio and surface roughness. For the range of the Reynolds number studied, the drag coefficient measured for the rigid test rods is approximately 0.95. Although the fluid model is simple, we expect that the complicated fluid mechanics and turbulence effects are reasonably accounted for by the drag measured on the rigid structure. The drag on a deformed rod is therefore written in integral form:

$$D = \frac{1}{2} \rho d C_D U^2 \int_0^L \sin^3(\theta(s)) ds \ . \quad (12)$$

A drag coefficient is sufficient to define the fluid loading since the lift and pitching moment coefficients are zero on a circular rod section. Consequently, all external moments in Eqn. 8 are null. The aerodynamic loading and the gravitational force on the rod are then decomposed into the  $x$ -,  $y$ - and  $z$ -directions of the material frame to obtain the external forces in Eqn. 7. By expanding Eqns. 7 and 8 in three directions and introducing the external forces and moments, the Kirchhoff equations

are written as:

$$\frac{dN_x}{ds} = N_y\tau - T\kappa_y - p_n.c_{11} - mgL^{-1}.c_{13} , \quad (13)$$

$$\frac{dN_y}{ds} = T\kappa_x - N_x\tau - p_n.c_{21} - mgL^{-1}.c_{23} , \quad (14)$$

$$\frac{dT}{ds} = N_x\kappa_y - N_y\kappa_x - mgL^{-1}.c_{33} , \quad (15)$$

$$\frac{d\kappa_x}{ds} = \frac{1}{(EI)_x} [(EI)_y\kappa_y\tau - GJ\kappa_y\tau + N_y] , \quad (16)$$

$$\frac{d\kappa_y}{ds} = \frac{1}{(EI)_y} [GJ\kappa_x\tau - (EI)_x\kappa_x\tau - N_x] , \quad (17)$$

$$\frac{d\tau}{ds} = \frac{1}{GJ} [(EI)_x\kappa_x\kappa_y - (EI)_y\kappa_x\kappa_y] . \quad (18)$$

To develop dimensionless equations of a deforming rod, the Cauchy number is introduced:

$$C_Y = C_D \frac{\rho U^2 L^3 d}{2(EI)_y} . \quad (19)$$

The Cauchy Number  $C_Y$  represents the ratio of the fluid force to the minimum bending rigidity of the flexible body (Chakrabarti, 2002; de Langre, 2008; Gosselin & de Langre, 2011). The square root of the Cauchy number is similar to the *dimensionless velocity* (Alben et al., 2002, 2004) or the *elasto-hydrodynamical number* (Schouveiler & Boudaoud, 2006) which do not include the drag coefficient in their definition.

The *reconfiguration number* (Gosselin et al., 2010) and similarly the *effective length* (Luhar & Nepf, 2011) represent the effect of flexibility on the drag force. The reconfiguration number is defined as the ratio of the drag force of the flexible body to the drag force of an equivalent rigid body:

$$\mathcal{R} = \frac{D}{\frac{1}{2}\rho U^2 C_D d L} . \quad (20)$$

It is a measure of the drag reduction of a flexible structure due to its flexibility. The Vogel exponent relates the Cauchy number (Eqn. 19) to the reconfiguration number (Gosselin et al., 2010) as:

$$\mathcal{R} \propto C_Y^{\frac{6}{5}} . \quad (21)$$

The *bending rigidity ratio*, is defined as:

$$\lambda = \frac{(EI)_y}{(EI)_x} , \quad (22)$$

where  $(EI)_y$  and  $(EI)_x$  are bending rigidities about the  $y$  and  $x$ -directions respectively. By definition, we take  $(EI)_y < (EI)_x$ . The flexible rods therefore have directional rigidity which causes a bending-torsion coupling when transverse loads are not aligned with the  $x$  or  $y$  axes. Based on the aforementioned directional rigidity, we redefine the twist-to-bend ratio (Eqn. 2) as:

$$\eta = \frac{(EI)_y}{GJ} . \quad (23)$$

The following dimensionless parameters are also required:

$$\begin{aligned} \bar{s} &= s/L & \bar{\kappa}_x &= \kappa_x L & \bar{\kappa}_y &= \kappa_y L & \bar{\tau} &= \tau L , \\ \bar{N}_x &= \frac{N_x L^2}{(EI)_y} & \bar{N}_y &= \frac{N_y L^2}{(EI)_y} & \bar{T} &= \frac{TL^2}{(EI)_y} & \mathcal{W} &= \frac{mgL^2}{(EI)_y} . \end{aligned}$$

By applying the external loading in the equations, the deformed shape of the rod's centerline (Eqn. 13 to 18) can be defined by the following six dimensionless equations:

$$\frac{d\bar{N}_x}{d\bar{s}} = \bar{N}_y \bar{\tau} - \bar{T} \bar{\kappa}_y - C_Y \sqrt{1 - c_{31}^2} \cdot c_{11} - \mathcal{W} \cdot c_{13} , \quad (24)$$

$$\frac{d\bar{N}_y}{d\bar{s}} = \bar{T} \bar{\kappa}_x - \bar{N}_x \bar{\tau} - C_Y \sqrt{1 - c_{31}^2} \cdot c_{21} - \mathcal{W} \cdot c_{23} , \quad (25)$$

$$\frac{d\bar{T}}{d\bar{s}} = \bar{N}_x \bar{\kappa}_y - \bar{N}_y \bar{\kappa}_x - \mathcal{W} \cdot c_{33} , \quad (26)$$

$$\frac{d\bar{\kappa}_x}{d\bar{s}} = \left( \lambda - \frac{\lambda}{\eta} \right) \bar{\kappa}_y \bar{\tau} + \lambda \bar{N}_y , \quad (27)$$

$$\frac{d\bar{\kappa}_y}{d\bar{s}} = \left( \frac{1}{\eta} - \frac{1}{\lambda} \right) \bar{\kappa}_x \bar{\tau} - \bar{N}_x , \quad (28)$$

$$\frac{d\bar{\tau}}{d\bar{s}} = \left( \frac{\eta}{\lambda} - \eta \right) \bar{\kappa}_x \bar{\kappa}_y . \quad (29)$$

As previously mentioned, the three direction cosines can be calculated from the six independent ones. Arbitrarily, using Eqn. 6, the six equations defining the  $x$ - and  $z$ -directions of the material frame are considered as the six independent equations. By coupling these six equations with Eqns. 24 to 29, the full state of a deforming rod can be defined. The set of twelve ordinary differential equations is solved with the `bvp4c` solver of MATLAB. The boundary conditions at the rod's free end ( $\bar{s} = 1$ ) and

the rod's fixed end ( $\bar{s} = 0$ ) are:

$$\begin{aligned}
\bar{N}_x(\bar{s} = 1) &= 0, & \bar{N}_y(\bar{s} = 1) &= 0, & \bar{T}(\bar{s} = 1) &= 0, \\
\bar{\kappa}_x(\bar{s} = 1) &= 0, & \bar{\kappa}_y(\bar{s} = 1) &= 0, & \bar{\tau}(\bar{s} = 1) &= 0, \\
c_{11}(\bar{s} = 0) &= \cos(\alpha_s) \cos(\psi_0), & c_{12}(\bar{s} = 0) &= \cos(\alpha_s) \sin(\psi_0), & c_{13}(\bar{s} = 0) &= -\sin(\alpha_s), \\
c_{31}(\bar{s} = 0) &= \sin(\alpha_s), & c_{32}(\bar{s} = 0) &= 0, & c_{33}(\bar{s} = 0) &= \cos(\alpha_s),
\end{aligned}$$

where  $\alpha_s$  is the rotation of the clamp due to the imperfect boundary condition evaluated with Eqn. 3. A continuation method is used to calculate the full state of the rod for a range of Cauchy numbers. In this method, the solver uses an initial guess for all twelve variables of the governing equations for a very small Cauchy number i.e.  $C_Y = 0.1$ . The solution of this step is then used as the initial guess for the next iteration for a higher Cauchy number. This procedure is repeated until the Cauchy number reaches its specified higher limit i.e.  $C_Y = 1000$ .

It is expected that the rod undergoes a bifurcation when  $\psi_0 = 90$ . However, the developed MATLAB code is unable to predict static instabilities for this angle of incidence because it cannot calculate and follow more than one branch of the solution. Thus, for  $\psi_0 = 90$ , a software package AUTO (Doedel & Kernevez, 1986) is used with the same aforementioned governing equations and boundary conditions. This software package has been developed to solve continuation and bifurcation problems. According to the Implicit Function Theorem (Inayat-Hussain et al., 2003), the system of ordinary differential equations presented in Eqn. 24 to Eqn. 29, has a stationary solution. In the software, using a successive continuation approach, the governing equations are solved starting from an initial known solution for a range of a continuation parameter values. In the present work, the Cauchy number is considered as the continuation parameter. Bifurcation points are detected by seeking the singularities in the Jacobian of the governing equations where eigenvalues change signs. A cross-comparison for cases with  $\psi_0 \neq 90$  between the MATLAB code and the AUTO solver shows identical results to 7 significant figures.

### 3. Results and Discussion

Three flexible rods made of polyurethane foam (Table 2) were tested in the wind tunnel to investigate the effect of bending and torsion on rod drag. In Fig. 5, highly contrasted photographs depict the frontal and side views of specimen R3 in the wind tunnel for three flow velocities and three angles

of incidence. In this figure, the thin solid lines represent the shape of an equivalent rod predicted using the mathematical model. The rod undergoes a two-dimensional bending or *in-plane* deformation for  $\psi_0 = 0$ . In this condition, the rod's material frame with the minimum bending rigidity  $(EI)_y$  is aligned with the flow therefore the reconfiguration is in pure bending. The magnitude of deformation increases with increasing flow velocity. For a non-zero angle of incidence, e.g.  $\psi_0 = 45$ , where the rod's material frame is not aligned with the flow, the magnitude of the in-plane deformation is smaller compared to the case  $\psi_0 = 0$ . This is due to the increasing contribution of the reinforcement fibers to the bending rigidity leading to less deformation. However, for non-zero angles of incidence, because of asymmetric bending, the rod undergoes a three-dimensional deformation showing both in-plane and *out-of-plane* deformation. This out-of-plane deformation creates a moment arm about the rod's root which twists the rod to realign it with the flow. For  $\psi_0 = 90$ , the rod's material frame is aligned with the flow but with the maximum bending rigidity  $(EI)_x$ . Because of symmetry, the rod does not show an out-of-plane deformation at  $10 \text{ ms}^{-1}$ . Compared with  $\psi_0 = 0$ , at  $\psi_0 = 90$  the deformation is smaller. At  $\psi_0 = 90$ , for larger flow velocities ( $U = 20, 30 \text{ ms}^{-1}$ ), the symmetry is broken and significant out-of-plane deformation is observed. In this case, the rod undergoes a supercritical and static pitchfork bifurcation which is discussed below. The difference between the experimental and mathematical results is mainly due to imperfect boundary conditions in the experiments.

Figure 6a shows the variation of the  $X$ -component displacement ( $X_{tip}$ ) of the tip of specimen R3 with increasing flow velocity for different angles of incidence. Experimental data points extracted from photographs are also presented with markers for reference. To visualize the out-of-plane deformation, the camera had to be placed inside the wind tunnel. Therefore, there are no experimental data points for flow velocities higher than  $30 \text{ ms}^{-1}$  due to technical limitations in taking photographs. For the three incidence angles, the  $X$ -component of the tip increases with flow velocity. However, the rate of increase of  $X_{tip}$  becomes considerably small for high velocities therefore  $X_{tip}$  asymptotically approaches a constant value. It is also seen that by increasing the angle of incidence, the magnitude of the in-plane deformation decreases. This is due to the increasing bending rigidity with the angle of incidence. Figure 6b shows the out-of-plane deformation of specimen R3 by providing the variation of the tip's  $Y$ -component displacement ( $Y_{tip}$ ) with velocity. For  $\psi_0 = 0$  the rod does not have an out-of-plane deformation, thus  $Y_{tip} = 0$ . For  $\psi_0 = 30, 45$  and  $60$ ,  $Y_{tip}$  variation shows an initial increase in the out-of-plane deformation. However, the experimental results and the mathematical predictions show that  $Y_{tip}$  starts to decrease as the rod twists back and becomes more aligned with the flow.

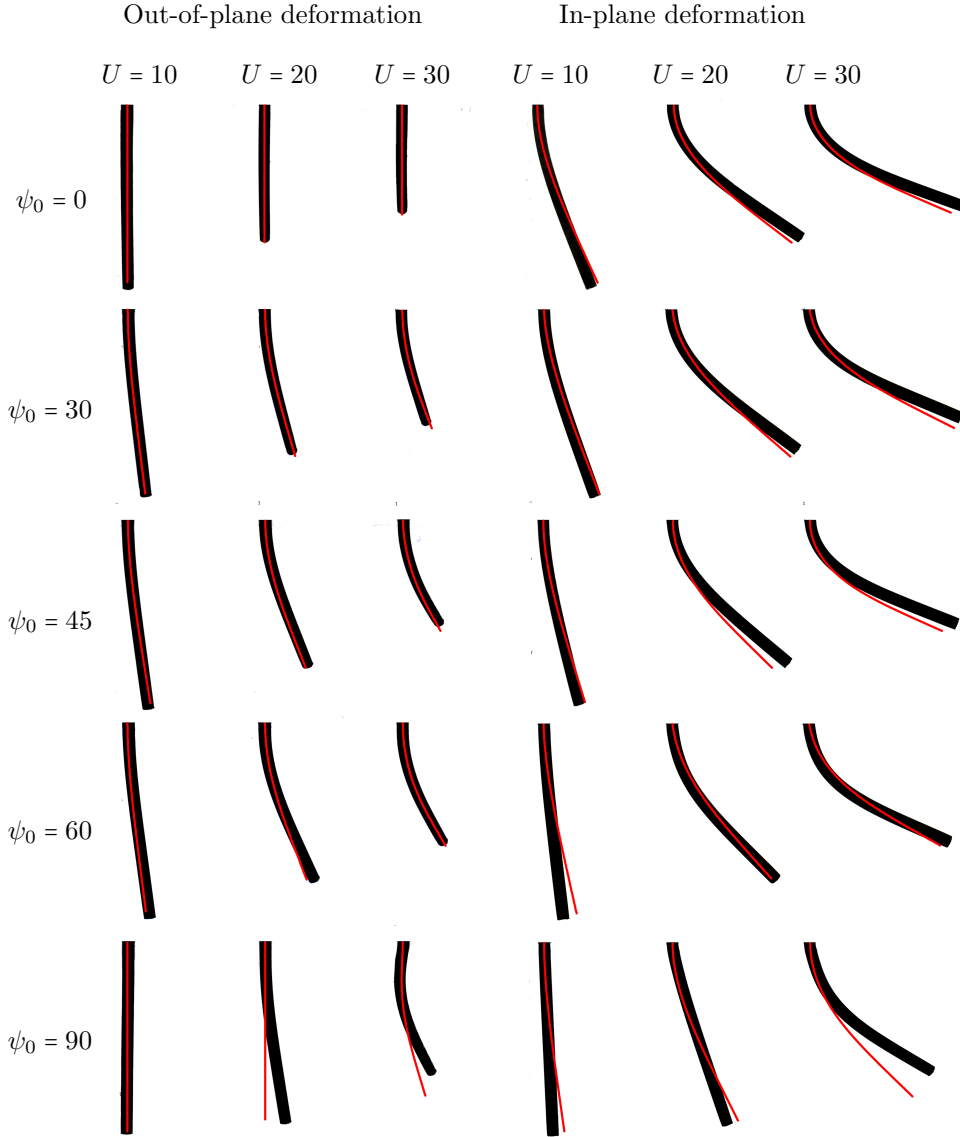


Figure 5: Photographs of deformed shapes of the specimen R3. Thin lines represent the deformation of an equivalent rod predicted by the mathematical model. The velocity units are  $\text{ms}^{-1}$ .

For  $\psi_0 = 90$ ,  $Y_{tip}$  is zero prior to a critical velocity of approximately  $26 \text{ ms}^{-1}$ , thus the rod does not undergo an out-of-plane deformation below this velocity. Beyond the critical velocity,  $Y_{tip}$  undergoes a jump to a maximum or minimum value approximately  $\pm 31 \text{ mm}$  exhibiting a pitchfork bifurcation.  $Y_{tip}$  then decreases with flow velocity showing the rod becoming aligned with the flow. Prior to the bifurcation point, the symmetric bending of the rod is stable but beyond that point, the rod loses its stability and jumps to a stable branch to either sides showing a sudden out-of-plane deformation. The post-bifurcation displacement is triggered by an infinitesimal out-of-plane deformation along with

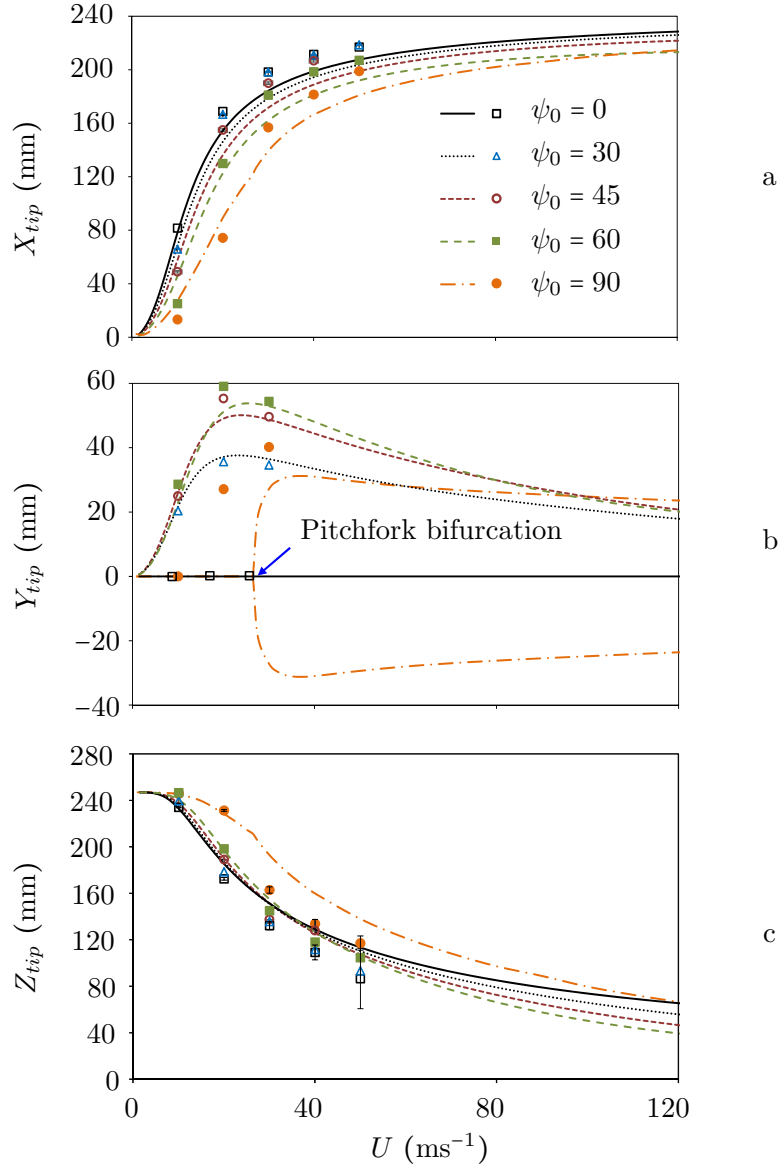


Figure 6: Mathematical evaluation of the in-plane and out-of-plane deformation of specimen R3 for three angles of incidence by showing a) the variation of the tip's  $X$ -component, b) the tip's  $Y$ -component and c) the tip's  $Z$ -component with flow velocity. Some experimental data points are provided for reference as markers. Error bars represent the standard deviation of the time fluctuations of the tip position.

the resulting moment arm about the root. This moment arm twists sections of the rod to an angle of incidence smaller than 90, inducing a larger out-of-plane deformation. The larger out-of-plane deformation amplifies the moment arm and this interaction continues until the rod finds a new three-dimensional equilibrium state. Similarly to Fig. 5, for  $\psi_0 = 90$ , the experimental and mathematical results are not in exact agreement due to imperfect boundary conditions in the experiments which advances the bifurcation.

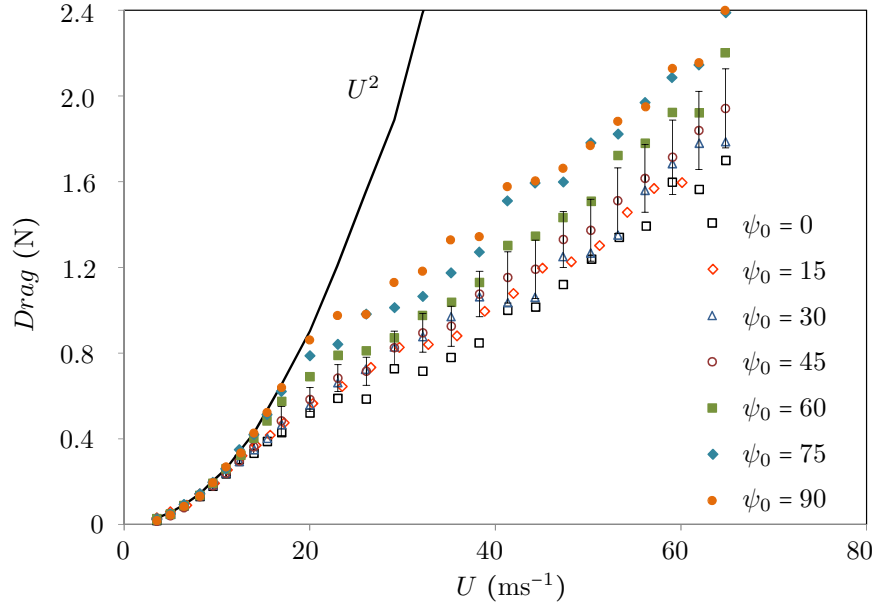


Figure 7: Time-averaged drag of the specimen R3 for a range of  $\psi_0$  from 0 to 90. Drag loading on an equivalent rigid rod is provided as a line for reference. Error bars represent the standard deviation of the time fluctuations for series  $\psi_0 = 45$ . Time fluctuations are similar for other series.

Figure 7 presents the variation of the measured drag of the specimen R3 with increasing flow velocity for a range of angles of incidence. The measured drag for an equivalent rigid structure is also shown for reference. The drag on the rod increases with the flow velocity as well as the angle of incidence. For low flow velocities, the drag on the flexible rod is similar to the drag force on an equivalent rigid structure following the  $U^2$  scaling curve. However, with increasing flow velocity, the drag force on the flexible rod increases in a less pronounced way than the equivalent rigid bar. This divergence from the  $U^2$  scaling results from the increase in the static deformation. The divergence is delayed by increasing the angle of incidence. Thus, the drag on the flexible rod increases monotonically with the angle of incidence because of the increasing contribution of fibers to the rod rigidity.

The twisting moment at the root ( $M_Z$ ), simply referred to as the torque hereafter, is a direct indicator of the magnitude of torsional reconfiguration. The torque is measured directly by the force transducer as the twisting moment about the  $Z$ -axis. Figure 8 shows the variation of the torque with flow velocity for a range of angles of incidence for R3. For  $\psi_0 = 0$ , the torque is null because there is no out-of-plane deformation to create a moment arm. For a non-zero angle of incidence, the torque remains approximately zero for low flow velocities since the rod does not deform significantly to create a moment arm. For  $U$  greater than approximately  $10 \text{ ms}^{-1}$ , the deformation of the rod creates a moment arm. The torque increases with increasing flow velocity as well as angle of incidence. This is

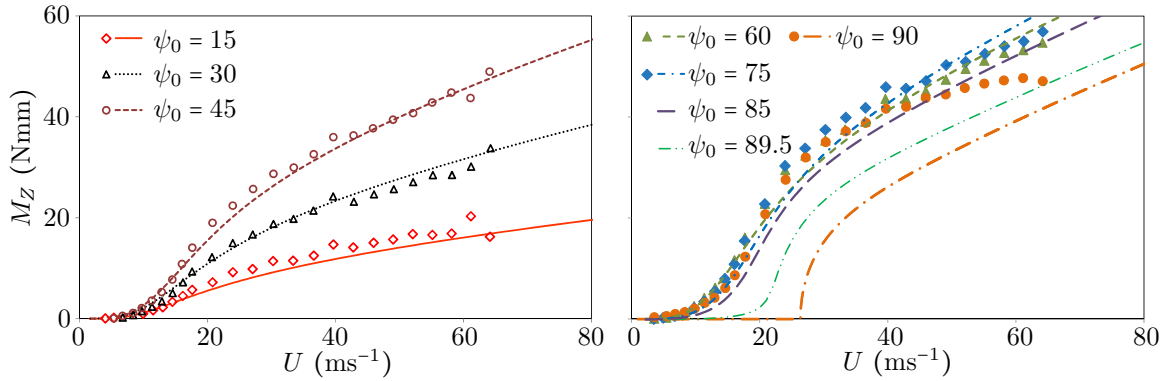


Figure 8: Twisting moment at the root of the specimen R3 varying by the flow velocity and angle of incidence. The mathematical evaluation of the root's twisting moment is provided as lines for reference.

due to the combined increase in the moment arm and fluid loading. The reinforced rods under study make it possible to control the amount of twisting reconfiguration by varying the angle of incidence.

In Fig. 8, the calculated torque for a rod equivalent to specimen R3 at the same angles is presented. The mathematical model shows a good agreement with the experiments for  $\psi_0 < 90$ . However, for  $\psi_0 = 90$ , the mathematical model is shifted as compared to the experimental data points. The mathematical model predicts that prior to a critical flow velocity of  $U \approx 27 \text{ ms}^{-1}$  the torque is null due to symmetric bending. Beyond this critical flow velocity, the symmetry is broken due to the rod undergoing a pitchfork bifurcation. The difference between the experimental and mathematical results for  $\psi_0 = 90$  is likely due to imperfect symmetry in the experiments which causes early bifurcation. This imperfect symmetry may be caused by an error in the angle of incidence, imperfect clamped boundary condition, heterogeneous mass distribution or a slight natural curvature in the rods. Fig. 8 shows that there is a limiting behavior which leads to a bifurcation at  $\psi_0 = 90$ . Moreover, the mathematical result for  $\psi_0 = 85$  represents a better agreement with the experimental results for  $\psi_0 = 90$ . This suggests that the combined effect of the aforementioned factors particularly the angle of incidence may lead to a large imperfection responsible for the inconsistency between the numerical and experimental results for  $\psi_0 = 90$ .

### 3.1. Dimensionless Representation

The system of equations 24 to 29 representing the arbitrary large deformation of a rod is rendered dimensionless by introducing the Cauchy number in Eqn. 19. From the experimental drag measurements, the variation of the reconfiguration number of the specimens R3 with increasing Cauchy number is presented in Fig. 9 for a range of  $\psi_0$  from 0 to 90 degrees. By definition, the dimensionless drag

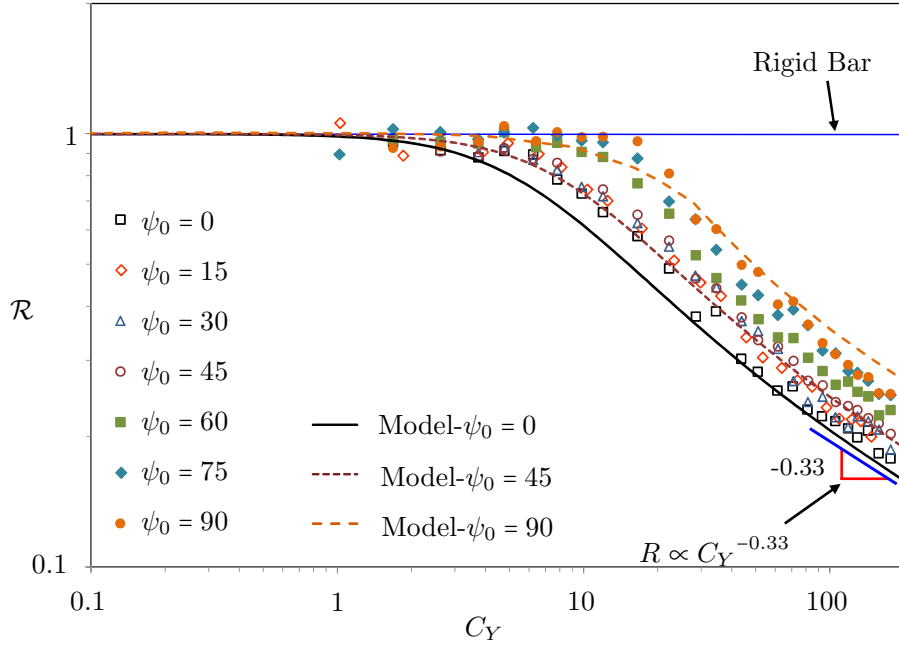


Figure 9: Experimental drag scaling of the specimen R3 represented by the Cauchy number and the reconfiguration number. The equivalent mathematical model for  $\psi_0 = 0, 45$  and  $90$  is provided as lines.

scaling of a rigid bar is presented with a horizontal line at  $\mathcal{R} = 1$  in this figure. It is seen that for small Cauchy numbers the reconfiguration number is approximately 1 which means that the drag force on the flexible rod is close to that acting on an equivalent rigid bar. Between  $C_Y \approx 3$  and 20, depending on the angle of incidence, the reconfiguration number starts to diverge from that of the equivalent rigid bar and decreases with increasing Cauchy number. This divergence is delayed by increasing the angle of incidence due to the increasing contribution of the fibers in the bending rigidity against the flow.

The variation of  $\mathcal{R}$  with  $C_Y$  calculated with the mathematical model is presented as lines in Fig. 9 for three angles of incidence. The reconfiguration number is 1 for small Cauchy numbers but it diverges from  $\mathcal{R} = 1$  for Cauchy numbers greater than unity. Similarly to the experimental measurements, the reconfiguration number decreases with the Cauchy number and increases with increasing angle of incidence. All experimental drag measurements in dimensionless form are found to fall between the two limiting mathematical curves for  $\psi_0 = 0$  and  $\psi_0 = 90$ .

For Cauchy numbers greater than 100, the experimental data points for each angle of incidence can be fitted with a power law which appears as a straight line on the  $\mathcal{R} - C_Y$  log-log plot. The slope of this line is the exponent of the power law. According to Eqn. 21, the Vogel exponent is twice this slope. In Fig. 9, the slope of  $-0.33$ , equivalent to  $\vartheta = -0.66$  expected for pure bending (Alben et al., 2002, 2004; Gosselin et al., 2010), is provided for reference. Table 3 presents the Vogel exponents

Table 3: The Vogel exponent for a range of angle of incidence calculated from the experimental data points and the mathematical simulation of R3

$\psi_0$	0	15	30	45	60	75	90
$\vartheta$ (Exp. $C_Y > 100$ )	-0.70	-0.62	-0.66	-0.66	-0.68	-0.86	-0.86
$\vartheta$ (Math. $100 < C_Y < 300$ )	-0.76	-0.76	-0.76	-0.76	-0.74	-0.74	-0.76
$\vartheta$ (Math. $300 < C_Y < 500$ )	-0.72	-0.72	-0.72	-0.72	-0.70	-0.68	-0.68
$\vartheta$ (Math. $500 < C_Y < 1000$ )	-0.7	-0.72	-0.72	-0.72	-0.70	-0.68	-0.68
Exp. Coeff. of Determination	0.88	0.85	0.76	0.97	0.82	0.94	0.95

calculated from the experimental data points for specimen R3 for different angles of incidence and  $C_Y > 100$ . The Vogel exponent is found to vary from -0.62 to -0.86 and the average coefficient of determination for the fitted data is 0.85. With the mathematical model, the predicted Vogel exponent does not change significantly with the variation of angle of incidence. It remains approximately  $-0.7$  for any angle of incidence and very high Cauchy numbers. However, in the experiments the predicted mathematical Vogel exponent is not reached for all angles of incidence because for higher angles, the maximum Cauchy number attainable in the wind tunnel is not sufficient to align the rod with the flow. The small difference between the predicted Vogel exponent in our mathematical model and that of previous studies in pure bending is due to the non-negligible weight of the rod in the present model (see Luhar & Nepf (2011)).

The torsion of a rod alters its effective bending rigidity in the flow direction for non-zero angles of incidence. The choice of  $(EI)_y$  is therefore not representative when computing the Cauchy number (Eqn. 19) for a non-zero angle of incidence. An alternative is proposed in the following which considers the effect of torsion on the bending rigidity and the Cauchy number.

### 3.2. Equivalent Bending Rigidity

We seek a modification to the Cauchy number to account for the effective bending rigidity which lies somewhere between  $(EI)_x$  and  $(EI)_y$ . This effective rigidity depends on the angle the material frame makes with the flow, thus it depends on the incidence angle  $\psi_0$  and the torsional rigidity. A dimensionless representation is proposed in the following which considers the effect of the angle of incidence and the rigidity ratios ( $\lambda$  and  $\eta$ ) on the equivalent bending rigidity and the Cauchy number.

The rigidity of a flexible rod comes from a contribution of the foam matrix and reinforcement fibers:

$$(EI)_{eq} = (EI)_{matrix} + (EI)_{fiber} . \quad (30)$$

For the configuration shown in Fig. 3, in the undeformed case and based on the parallel axis theorem,

the equivalent bending rigidity is written as:

$$(EI)_{eq} = (EI)_{matrix} + E_f \sum_1^{n_f} I_{f,0} + A_f (r \sin \psi_0)^2 . \quad (31)$$

where  $r$  is the radial distance of each fiber from the rod's centerline,  $A_f$  is the fiber sectional area,  $n_f$  is the number of fibers and  $I_{f,0}$  is the second moment of area of each fiber around its neutral axis. Since the fibers are very thin relative to the rods,  $E_f I_{f,0}$  is negligible. Therefore the bending rigidity around the two directions of the material frame can be approximated as:

$$(EI)_y \approx (EI)_{matrix} , \quad (32)$$

$$(EI)_x \approx (EI)_{matrix} + E_f \sum_1^{n_f} A_f r^2 . \quad (33)$$

By subtracting Eqn. 32 from Eqn. 33 and introducing the result into Eqn. 31, the equivalent bending rigidity can be written as:

$$(EI)_{eq} = (EI)_y + [(EI)_x - (EI)_y] \sin^2 \psi_0 , \quad (34)$$

where  $[(EI)_x - (EI)_y] \sin^2 \psi_0$  is the contribution of the reinforcement fibers in the equivalent bending rigidity. This could be an improved definition of the bending rigidity to construct the Cauchy number. However, according to Eqn. 18 the reinforced rod twists proportionally to:

$$\zeta = \frac{(EI)_x - (EI)_y}{GJ} = \frac{\eta}{\lambda} (1 - \lambda) . \quad (35)$$

As a result, the equivalent bending rigidity of the rod varies with the twist angle. When the rod bends in the flow, it also reorients to bend in its most flexible direction by aligning the  $x$ -direction of the material frame with the flow. Therefore the angle of incidence at each section of the rod may become smaller than the initial angle of incidence  $\psi_0$ . This decreases the contribution of the reinforcement fibers in the bending rigidity and consequently reduces the overall bending rigidity of the rod. We therefore propose the following ansatz for an improved equivalent bending rigidity definition:

$$(EI)_{eq} = (EI)_y + \frac{[(EI)_x - (EI)_y] \sin^2 \psi_0}{1 + \zeta^\beta} , \quad (36)$$

where  $\beta > 0$  is an exponent to be defined. In Eqn. 36, the bending-torsion coupling parameter  $\zeta$  varies

the contribution of the reinforcement fibers in the equivalent bending rigidity. If  $\zeta \ll 1$ , the rod is rigid in torsion and the correction found in Eqn. 34 holds. If  $\zeta \gg 1$ , the rod twists freely, it reorients under the slightest load to bend in its most flexible direction and  $(EI)_{eq} \approx (EI)_y$ . Assuming small deformations, the curvatures  $\kappa_x$  and  $\kappa_y$  are approximated as:

$$\kappa_x = \frac{d^2 (w_{eq} \sin \psi_0)}{ds^2}, \quad (37)$$

$$\kappa_y = \frac{d^2 (w_{eq} \cos \psi_0)}{ds^2}, \quad (38)$$

where  $w_{eq}$  is the deformation in the flow direction due to a uniform pressure. This deformation is calculated from linear Euler-Bernoulli beam theory as:

$$w_{eq} = \frac{p_n s^2 [6L^2 - 4Ls + s^2]}{24(EI)_{eq}}. \quad (39)$$

The equivalent bending rigidity is a bulk property. By substituting Eqn. 37, 38 and 39 in Eqn. 18 and rewriting it in integral form, we obtain the average twist:

$$\begin{aligned} \tau_{avg} &= \frac{1}{2} \zeta \sin(2\psi_0) \int_0^L \left( \frac{d^2 w_{eq}}{ds^2} \right)^2 ds \\ &= \frac{p_n^2}{40} L^5 \sin(2\psi_0) \frac{\zeta}{[(EI)_{eq}]^2}, \end{aligned} \quad (40)$$

Equation 40 shows that for a given load, the average twist remains constant if  $(EI)_{eq} \propto \zeta^{1/2}$  which leads us to choose  $\beta = 1/2$ . An *equivalent Cauchy number* is then defined as:

$$C_Y^* = C_D \frac{\rho U^2 L^3 d}{2(EI)_{eq}}, \quad (41)$$

The variation of  $\mathcal{R}$  with  $C_Y$  (Eqn. 19) for the three flexible rods (Table 2) and for a range of angle of incidence from 0 to 90 is presented in Fig. 10a. As seen in the figure, the reconfiguration number is approximately 1 for all three specimens for small Cauchy numbers, which means that the drag is close to that of the equivalent rigid bar. Starting from mid-range Cauchy numbers between  $C_Y \approx 5$  and 20, the reconfiguration number decreases with increasing Cauchy number. The maximum reachable Cauchy number is less than 100 for the rods R1 and R2 due to the limitation of the test equipment. The slope of the log-log plot is therefore less than -0.33 for these two specimens. The

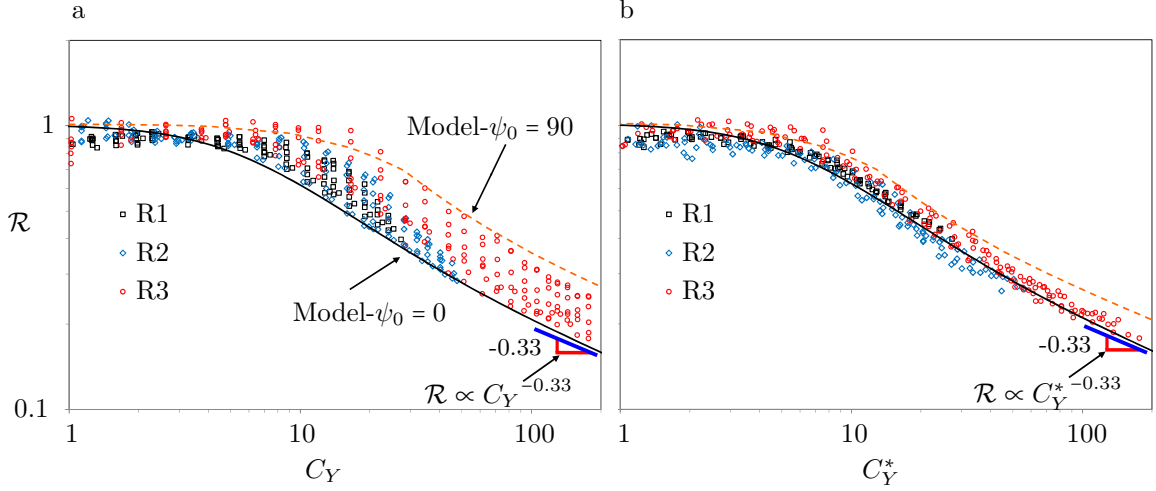


Figure 10: The reconfiguration number of the three specimens (table 2) for a range of  $\psi$  between 0 and 90 plotted versus a) the Cauchy number and b) the equivalent Cauchy number to find a generic representation of the drag scaling. The Mathematical models for  $\psi_0 = 0$  and  $\psi_0 = 90$  are presented as lines.

variation of  $\mathcal{R}$  with  $C_Y$  using the mathematical model is presented as lines for R3 in Fig. 10a. It is found that all the experimental drag measurements fall between the two limiting curves for  $\psi_0 = 0$  and 90. However, the measurements for the three specimens do not collapse on a single curve.

Figure 10b presents the dimensionless drag measurements for all three specimens obtained using the equivalent Cauchy number (Eqn. 41) for the range of angles of incidence from 0 to 90. The results show that the reconfiguration number is approximately 1 for small equivalent Cauchy numbers and starts to diverge from  $\mathcal{R} = 1$  near  $C_Y^* \approx 2$  to 8. It decreases with increasing equivalent Cauchy number and a constant power law exponent is reached for large equivalent Cauchy numbers. In the figure, the  $\mathcal{R} - C_Y^*$  plots of the mathematical model for specimen R3 for  $\psi_0 = 0$  and 90 are presented for reference. As shown, all experimental results effectively collapse onto a single curve regardless of test conditions. The single curve, representing the two-dimensional bending deformation for  $\psi_0 = 0$ , can quantify the drag scaling of bending and twisting rods independently of their geometry, material properties and angle of incidence. This means that using the right set of dimensionless numbers ( $\mathcal{R}$  and  $C_Y^*$ ), the three-dimensional reconfiguration of a rod and the bending deformation of a beam are similar, both governed by a single parameter ( $C_Y^*$ ). In this representation, the Vogel exponent of a bending-twisting rod approaches the Vogel exponent of the two-dimensional bending case, -0.66.

To have a better understanding of the torsion of the rod along its length, the variation of the dimensionless twist ( $\bar{\tau}$ ) along the dimensionless length of the rod is studied using the mathematical model. The dimensionless twist represents the variation of the sectional angle of incidence. Figure 11

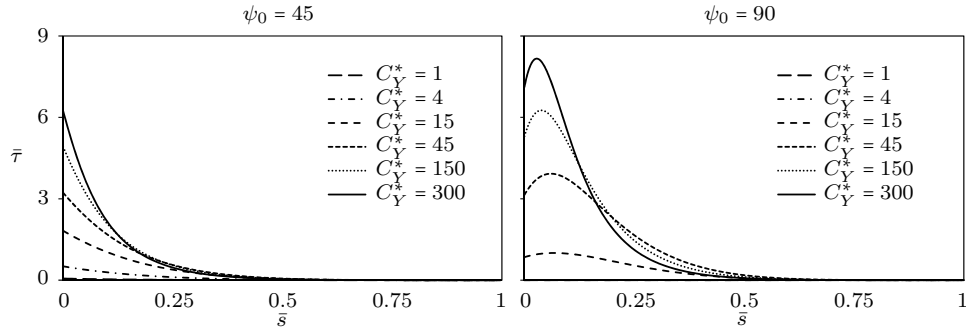


Figure 11: Mathematical demonstration of torsion of R3 along its length by plotting the variation of  $\bar{\tau}$  with  $\bar{s}$ ,  $C_Y^*$  and  $\psi_0$ .

shows the variation of the dimensionless twist for specimen R3 along its length for small to very high equivalent Cauchy numbers and two angles of incidence. This figure is an illustration of the magnitude of torsion at each section of the rod. By definition, the area under each curve in Fig. 11 gives the total twist angle of the rod's tip relative to its root.

The figure shows that most of the torsion occurs close to the fixed end of the rod. In addition, as the equivalent Cauchy number increases, the generated torsion also increases close to the fixed end. The reason being that as the Cauchy number increases, sections of the rod far from the fixed end become aligned with the flow. As a result, no significant moment arm is created about these sections. At the same time, this aligned part of the rod acts as a moment arm for the sections close to the fixed end. As the equivalent Cauchy number increases, more sections become aligned with the flow increasing the torsion near the fixed end. In general,  $\bar{\tau}$  at the rod's root increases with the equivalent Cauchy number due to increasing fluid loading and out-of-plane deformation. For  $\psi_0 = 45$ , the maximum dimensionless twist is found at the fixed end of rod. However, for  $\psi_0 = 90$ , the location with the maximum torsion is found within the first quarter of the rod; the maximum torsion location then moves towards to the fixed end as the equivalent Cauchy number increases. The reason is probably due to the non-uniform out-of-plane deformation of the rod for  $\psi_0 = 90$  (see for instance Fig. 5). As seen in Fig. 5, generally the rod has an out-of-plane deformation towards the right side. However, for  $\psi_0 = 90$  and  $U = 30 \text{ m.s}^{-1}$  ( $\approx C_Y^* = 30$ ), the rod deforms to the left up to a certain point along its length and beyond this point, it twists and bends to the right. Thus, for  $\psi_0 = 90$ ,  $\bar{\tau}_{max}$  is found close to this turning point rather than the root. This also explains the reduction of the torque for  $\psi_0 = 90$  compared to the smaller angles in Fig. 8 since the torque at the root in  $\psi_0 = 90$ , is not the maximum twisting moment along its length.

To better understand the rod's twist, the following torsion length ( $\ell$ ) is proposed:

$$\ell = \frac{GJ\psi_0}{M_z L}, \quad (42)$$

where  $\psi_0$  is in radians. The torsion length  $\ell$  is the dimensionless length the rod would need to twist by an angle  $\psi_0$  under the torque  $M_z$  measured at its root. Figure 12 shows the variation of the torsion length of specimen R3 with increasing equivalent Cauchy number on a logarithmic scale. For small  $C_Y$ , the torsion length is large and thus the rod does not twist to align itself with the flow. With increasing equivalent Cauchy number, the torsion length decreases, corresponding to an increase in torsion. As  $C_Y$  is increased further,  $\ell$  becomes smaller than unity. The rod can thus align its most flexible direction with the flow and the torsion increases and becomes more localized at the root. This is due to the increasing out-of-plane deformation and moment arm magnitude which lead to a larger torque. Once the rod is twisted and aligned with the flow, the rod shows a reconfiguration similar to a bending beam. For  $\psi_0 = 90$ , the torsion length is infinite prior to the bifurcation because the deformation is symmetric, but the torsion length decreases suddenly beyond a critical equivalent Cauchy number. Once the bifurcation occurs, a moment arm is created which leads to a larger torque and smaller torsion length. As seen in Fig. 12, in the asymptotic regime of large deformation, the torsion length scales as  $\ell \propto C_Y^*{}^{-0.33}$ . This is interesting because as we observed in Fig. 10, the same scaling emerges for  $\mathcal{R}$  as a function of  $C_Y^*$ .

#### 4. Conclusion

The three-dimensional reconfiguration of plants was studied using flexible rods with structural anisotropy. The work aims to answer the following question: What is the effect of torsion on reconfiguration? It was shown that reinforcing the flexible rods in one direction leads to coupling between torsional and bending deformation. This allowed us to benefit from the simplicity of circular rods while being able to alter the bend-twist coupling. As observed in the experiments, the drag scaling of a flexible rod diverges from a  $U^2$  relation with increasing magnitude of deformation.

It was shown that the direction of reinforcement with respect to the flow ( $\psi_0$ ) is a key parameter in the effective bending rigidity of the rod. Based on this parameter, the definition of the Cauchy number was modified by introducing an equivalent bending rigidity. It was concluded that the equivalent Cauchy number and the reconfiguration number effectively characterize the three-dimensional

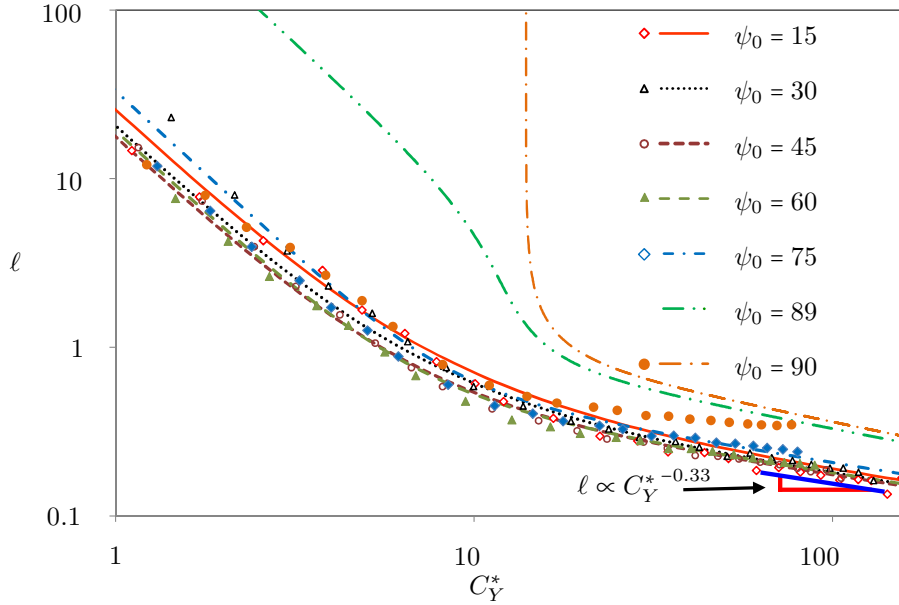


Figure 12: Experimental evaluation of the torsion length of specimen R3 varying with the equivalent Cauchy number. The mathematical model is provided as lines for comparison.

reconfiguration of the rod as a beam undergoing a two-dimensional bending.

The Vogel exponent of the reconfiguring rod approaches  $-0.7$  which is the exponent of bending beams and plates considering their weight. This shows that the three-dimensional reconfiguration of the rod becomes approximately two-dimensional in the regime of very large deformations. It is concluded that in the large deformation regime, torsion has no effect on the Vogel exponent since the exponent was found to be independent of the angle of incidence.

A mathematical model was developed by coupling the Kirchhoff theory of rods with a semi-empirical drag formulation. The model predicted that the Vogel exponent reaches  $-0.7$  for high Cauchy numbers independently of the angle of incidence, the rod's material and geometrical characteristics. A pitchfork bifurcation was also predicted for  $\psi_0 = 90$ . However, due to imperfect symmetry and flow perturbations in the experiments, the mathematical model overestimated the critical velocity at which bifurcation occurs. It would be interesting to evaluate and implement the imperfection of the boundary conditions to obtain a better prediction of the bifurcation.

While this paper focused on the effect of torsion on the reconfiguration of flexible rods, studying the three-dimensional reconfiguration of slender lifting surfaces might be of interest. In addition, the present work considers a rod which is initially undeformed. It would be of interest to study the reconfiguration of a rod with a pre-twisted material frame along its length. This case can be found in

the structure of many plants with chiral morphology.

### **Acknowledgment**

The authors are thankful to Benedict Besner and Nour Aimene for their technical support and Michael Plante, Diego Altamirano, Pablo Maceira-Elvira and Anthony Salze for their work on preliminary versions of the experimental setup. The financial support of the Natural Sciences and Engineering Research Council of Canada is acknowledged.

## Appendix 1

The direction cosines are a representation of the material frame's rotation. They are the cosines of the angles between a vector and the three directions forming the fixed coordinate system. Since the material frame and the fixed frame have three directions each, nine direction cosines are needed to define the material frame. As detailed by Audoly & Pomeau (2010), the spatial derivative of  $\mathbf{e}_i(s)$  with respect to  $s$  is defined by:

$$\mathbf{e}'_i(s) = \boldsymbol{\Omega}(s) \times \mathbf{e}_i(s) , \quad (43)$$

where  $i = x, y$  and  $z$ . The parameter  $\boldsymbol{\Omega}(s)$  is the rotation velocity or the *Darboux vector* defined by:

$$\boldsymbol{\Omega}(s) = \kappa_x(s)\mathbf{e}_x(s) + \kappa_y(s)\mathbf{e}_y(s) + \tau(s)\mathbf{e}_z(s) . \quad (44)$$

By introducing Eqn. 44 in Eqn. 43, spatial derivatives of the directions of the material frame are calculated as Eqn. 6. Each direction of the material frame is defined by the vector contained in a row of the matrix  $[c]$  (Eqn. 6), e.g.  $\mathbf{e}_x = (c_{11}, c_{12}, c_{13})$ . Therefore, by expanding Eqn. 6, we have:

$$\frac{dc_{11}}{ds} = \tau c_{21} - \kappa_y c_{31} \quad \frac{dc_{12}}{ds} = \tau c_{22} - \kappa_y c_{32} \quad \frac{dc_{13}}{ds} = \tau c_{23} - \kappa_y c_{33} , \quad (45)$$

$$\frac{dc_{21}}{ds} = -\tau c_{11} + \kappa_x c_{31} \quad \frac{dc_{22}}{ds} = -\tau c_{12} + \kappa_x c_{32} \quad \frac{dc_{23}}{ds} = -\tau c_{13} + \kappa_x c_{33} , \quad (46)$$

$$\frac{dc_{31}}{ds} = \kappa_y c_{11} - \kappa_x c_{21} \quad \frac{dc_{32}}{ds} = \kappa_y c_{12} - \kappa_x c_{22} \quad \frac{dc_{33}}{ds} = \kappa_y c_{13} - \kappa_x c_{23} . \quad (47)$$

## References

- Alben, S., Shelley, M., & Zhang, J. (2002). Drag reduction through self-similar bending of a flexible body. *Nature*, *420*, 479–481.
- Alben, S., Shelley, M., & Zhang, J. (2004). How flexibility induces streamlining in a two-dimensional flow. *Physics of Fluids*, *16*, 1694.
- Audoly, B., & Pomeau, Y. (2010). *Elasticity and geometry: from hair curls to the non-linear response of shells*. Oxford University Press Oxford.
- Berry, P. M., Sterling, M., Spink, J. H., Baker, C. J., Sylvester-Bradley, R., Mooney, S. J., Tams, A. R., & Ennos, A. R. (2004). Understanding and reducing lodging in cereals. *Advances in Agronomy*, *84*, 217–271.
- Chakrabarti, S. K. (2002). *The theory and practice of hydrodynamics and vibration* volume 20. World scientific.
- De Goeij, W., Van Tooren, M., & Beukers, A. (1999). Implementation of bending-torsion coupling in the design of a wind-turbine rotor-blade. *Applied Energy*, *63*, 191–207.
- Dill, E. H. (1992). Kirchhoff’s theory of rods. *Archive for History of Exact Sciences*, *44*, 1–23.
- Doedel, E., & Kernevez, J. P. (1986). *AUTO, software for continuation and bifurcation problems in ordinary differential equations*. California Institute of Technology.
- Eloy, C. (2011). Leonardos rule, self-similarity, and wind-induced stresses in trees. *Physical review letters*, *107*, 258101.
- Ennos, A. (1993). The mechanics of the flower stem of the sedge *Carex acutiformis*. *Annals of Botany*, *72*, 123–127.
- Ennos, A., Spatz, H.-C., & Speck, T. (2000). The functional morphology of the petioles of the banana, *Musa textilis*. *Journal of Experimental Botany*, *51*, 2085–2093.
- Etnier, S., & Vogel, S. (2000). Reorientation of daffodil (*Narcissus*: Amaryllidaceae) flowers inwind: drag reduction and torsional flexibility. *American Journal of Botany*, *87*, 29–32.
- Gosselin, F. P., & de Langre, E. (2011). Drag reduction by reconfiguration of a poroelastic system. *Journal of Fluids and Structures*, *27*, 1111–1123.

- Gosselin, F. P., de Langre, E., & Machado-Almeida, B. A. (2010). Drag reduction of flexible plates by reconfiguration. *Journal of Fluid Mechanics*, *650*, 319.
- Inayat-Hussain, J., Kanki, H., & Mureithi, N. (2003). On the bifurcations of a rigid rotor response in squeeze-film dampers. *Journal of fluids and structures*, *17*, 433–459.
- Koehl, M. A., & Alberte, R. (1988). Flow, flapping, and photosynthesis of *nereocystis luetkeana*: a functional comparison of undulate and flat blade morphologies. *Marine Biology*, *99*, 435–444.
- de Langre, E. (2008). Effects of wind on plants. *Annual Review of Fluid Mechanics*, *40*, 141–168.
- Lazarus, A., Miller, J., & Reis, P. (2013). Continuation of equilibria and stability of slender elastic rods using an asymptotic numerical method. *Journal of the Mechanics and Physics of Solids*, *61*, 1712–1736.
- Lopez, D., Michelin, S., & de Langre, E. (2011). Flow-induced pruning of branched systems and brittle reconfiguration. *Journal of Theoretical Biology*, *284*, 117–24.
- Love, A. E. H. (1944). *A Treatise on the Mathematical Theory of Elasticity*. (4th ed.). New York: Dover Publications.
- Luhar, M., & Nepf, H. M. (2011). Flow-induced reconfiguration of buoyant and flexible aquatic vegetation. *Limnology and Oceanography*, *56*, 2003–2017.
- Niklas, K. J. (1998). The influence of gravity and wind on land plant evolution. *Review of Palaeobotany and Palynology*, *102*, 1–14.
- Pasini, D., & Mirjalili, V. (2006). The optimized shape of a leaf petiole, . (pp. 35–45).
- Rudnicki, M., Mitchell, S. J., & Novak, M. D. (2004). Wind tunnel measurements of crown streamlining and drag relationships for three conifer species. *Canadian Journal of Forest Research*, *34*, 666–676.
- Schouveiler, L., & Boudaoud, A. (2006). The rolling up of sheets in a steady flow. *Journal of Fluid Mechanics*, *563*, 71.
- Skatter, S., & Kuera, B. (1997). Spiral grainan adaptation of trees to withstand stem breakage caused by wind-induced torsion. *Holz als Roh-und Werkstoff*, *55*, 207–213.
- Sterling, M., Baker, C., Berry, P., & Wade, A. (2003). An experimental investigation of the lodging of wheat. *Agricultural and Forest Meteorology*, *119*, 149–165.

- Taylor, G. (1952). Analysis of the swimming of long and narrow animals. *Proceedings of the Royal Society A: Mathematical, Physical and Engineering Sciences*, *214*, 158–183.
- Vogel, S. (1984). Drag and flexibility in sessile organisms. *American Zoologist*, *24*, 37–44.
- Vogel, S. (1989). Drag and reconfiguration of broad leaves in high winds. *Journal of Experimental Botany*, *40*, 8.
- Vogel, S. (1992). Twist-to-bend ratios and cross-sectional shapes of petioles and stems. *Journal of Experimental Botany*, *43*, 1527–1532.
- Vogel, S. (2007). Living in a physical world xi. to twist or bend when stressed. *Journal of Biosciences*, *32*, 643–655.
- Vollinger, S., Mitchell, S. J., Byrne, K. E., Novak, M. D., & Rudnicki, M. (2005). Wind tunnel measurements of crown streamlining and drag relationships for several hardwood species. *Canadian Journal of Forest Research*, *35*, 1238–1249.